## **ORIGINAL PAPER**



# Laboratory Evaluation of the Thermal Breakout Method for Maximum Horizontal Stress Measurement

Maciej Trzeciak<sup>1</sup> · Hiroki Sone<sup>1</sup> · Samuel Voegeli<sup>2</sup> · Charlotte E. Bate<sup>1</sup> · Herbert Wang<sup>1</sup>

Received: 10 February 2021 / Accepted: 10 August 2021 © The Author(s), under exclusive licence to Springer-Verlag GmbH Austria, part of Springer Nature 2021

#### Abstract

Measuring in situ stress is essential for many problems in geomechanics, and the maximum horizontal stress is the most difficult to constrain. We are developing an extension of the breakout method to measure maximum horizontal stress in regions where natural breakouts do not occur. In the novel thermal breakout method, additional compression which leads to breakout development is induced by heating the borehole wall. In the present study, we validated the method experimentally in a true-triaxial apparatus on samples with predrilled boreholes. Two rocks were selected for laboratory testing: high-porosity Berea sandstone and low-porosity Niagaran dolomite. Prior to main true-triaxial tests, we carried out standard testing to characterize the strength, elasticity and thermal properties. The true-triaxial experiments consisted of: (1) room-temperature tests where samples were first loaded mechanically until the breakout formed, and (2) elevated-temperature tests where samples were loaded mechanically within the elastic range with additional compression induced thermally. Breakout initiation was monitored by acoustic emission sensors mounted on the pistons that applied horizontal stresses. The magnitude of induced thermal stress was calculated from temperature measurements around the borehole wall. In both rock types, we created thermally induced breakouts and examined analytical expressions to constrain maximum horizontal stress based on strength, elastic and thermal properties of the rocks.

Keywords Thermal breakouts · Stress measurement · True-triaxial testing · Acoustic emission

# **List of Symbols**

a	Borehole radius (m)
$A_i$	Amplitude of first arrival at ith AE sensor
α	Linear coefficient of thermal expansion (1/K)
BCS	Borehole compressive strength (Pa)
$C_0$	Uniaxial compressive strength (Pa)
$C_1$	Strength in biaxial extension (Pa)
$C_p$	Specific heat (J/(K kg)
$\vec{E}$	Young's modulus (Pa)
k	Thermal conductivity (W/(m K))
$\nu$	Poisson's ratio (–)
$P_0$	Pore pressure (Pa)
$\Delta P$	Difference between mud weight and pore pressure
	(Pa)
r	Radial distance from center of the borehole (m)

 $<sup>\</sup>sigma_1$  Maximum principal stress (Pa)

 $\sigma_2$  Intermediate principal stress (Pa)  $\sigma_3$  Minimum principal stress (Pa)

 $\sigma_{\rm H}$  Maximum horizontal stress (Pa)  $\sigma_{\rm h}$  Minimum horizontal stress (Pa)

 $\sigma_{\rm v}$  Vertical stress (Pa)

 $\sigma_{\theta\theta}$  Circumferential (hoop) stress (Pa)

 $\sigma_{rr}$  Radial stress (Pa)

 $\sigma_{zz}$  Axial stress (in the direction of borehole axis) (Pa)

 $\sigma_{\rm oct}$  Normal octahedral stress (Pa)  $\tau_{\rm oct}$  Shear octahedral stress (Pa)

 $\Delta T$  Temperature change (K)

 $\theta$  Angle measured from the direction of maximum

horizontal stress

UCS Uniaxial compressive strength (Pa)

Published online: 04 October 2021

# 1 Introduction

Knowledge of in situ stress is essential for geological engineering applications including borehole stability analysis, hydraulic fracturing design, CO<sub>2</sub> sequestration, tunneling or



Maciej Trzeciak trzeciak2@wisc.edu

University of Wisconsin-Madison, 1415 Engineering Drive, Madison, WI, USA

RESPEC, 3824 Jet Drive, Rapid City, SD, USA

rock slope stability (e.g. Jaeger et al. 2007; Economides and Nolte 2000; Zoback 2007; Fjær et al. 2008). Also, it gives important insight into the geodynamics of a given region and facilitates tectonic interpretations (Zoback 1992; Heidbach et al. 2010). Therefore, the development of stress measurement methods is of central importance in geomechanics.

For simplicity of argument, it is commonly assumed that one of the principal stresses is vertical, and the other two are horizontal. Thus, the stress analysis consists of estimation of the principal stress magnitudes, and maximum horizontal stress direction (e.g. Zoback et al. 2003). The vertical stress is easily constrained by density log integration; the minimum horizontal stress can be estimated from extended leakoff tests or hydraulic fracturing tests (De Bree and Walters 1989); and the maximum horizontal stress direction is also relatively well-constrained from wellbore failures: breakouts and drilling induced tensile fractures, which form in the direction of minimum and maximum horizontal stresses. respectively. The most challenging component of in situ stress analysis is the maximum horizontal stress magnitude. Several methods have been proposed, and will be briefly reviewed below.

The overcoring stress measurement method relies on elastic rebound of rock when stress is released and it consists of three main steps (Amadei and Stephansson 1997): (1) small diameter borehole is drilled, (2) strain measurement device is installed inside, (3) the rock with the device is overcored using a larger diameter drill bit. At the moment of overcoring the stress is released, and the rock deformation is recorded by strain gauges. The stress change due to overcoring is calculated assuming linear elasticity. The widely used overcoring devices are the CSIRO hollow inclusion (HI) cell (Worotnicki 1993), USBM (Hooker and Bickel 1974; ISRM 1987), or Borre probe (Sjöberg et al. 2003). The deficiency of the method is that it relies on the assumption of linear elasticity of rocks which can be easily violated. Anisotropy introduces additional difficulty in accurate data analysis. Also, the strain gauges measure the deformation in very small areas, and any stress or rock heterogeneity greatly influences the final stress estimation. Finally, overcoring cannot be easily deployed at greater depths (> 1 km) and it is mostly used in shallow mining/civil engineering applications (e.g. Clement et al. 2009).

The hydraulic testing on pre-existing fractures (HTPF) method has been developed by Cornet (1983, 1986) (for a thorough description see Haimson and Cornet (2003)). In this method, a natural, pre-existing fracture is located using a scanning tool, the borehole interval containing it is sealed and the fracture is pressurized. Analysis of reopening pressures of fractures in different directions provides a method to constrain the entire stress tensor. The experimental results of the HTPF method have been presented by: Cornet and Burlet

(1992); Cornet and Jianmin (1995), Cornet et al. (2003) and Wileveau et al. (2007). The shortcoming of the method is that it assumes negligible percolation of hydraulic fluid into the rock matrix, and that the stress state is homogeneous. It also requires the presence of fractures in various orientations within the investigated borehole interval.

In the sleeve fracturing method (Stephansson 1983; Serata et al. 1992), a rubber sleeve is introduced into the borehole, the interval is sealed, and the sleeve is pressurized. When the pressure exceeds the minimum circumferential stress plus the rock tensile strength, a fracture forms in the azimuth of maximum horizontal stress ( $\sigma_H$ ). Contrary to the standard hydraulic fracturing tests, the fracture is very short, because it is constrained by the maximum expansion of the sleeve. The development of the first fracture releases the stress concentration in the  $\sigma_{\rm H}$  direction and upon further pressurizing the next fracture opens in the azimuth of minimum horizontal stress ( $\sigma_h$ ). From closing and reopening pressures of the two sets of fractures it is possible to constrain both horizontal stress magnitudes. However, as the induced fractures are short, near borehole stress perturbation and structural heterogeneity can make the far-field stress characterization difficult.

The methods described above provide means to measure the maximum horizontal stress magnitude. However, each of them has its shortcomings and related technical difficulties, which impede their standard use in deep boreholes. Most frequently, for deep boreholes, the maximum horizontal stress magnitude is constrained from borehole breakout analysis (e.g. Zoback et al. 1985; Moos and Zoback 1990, 1993; Lund and Zoback 1999; Jarosiński 2005; Chang et al. 2010; Malinverno et al. 2016). On the walls of a circular, vertical borehole the far field stress is amplified, and maximum compression is induced 90° from the direction of maximum far field horizontal stress (see Sect. 2.1 for details). If the stress-concentration reaches the rock strength, the borehole wall fails and a breakout is created. In the simplest approach and under the assumption of zero borehole effective radial stress, the failure is governed by the circumferential (hoop) stress only. Therefore, the uniaxial compressive strength (UCS) is commonly used as a measure of borehole strength. The maximum horizontal stress is estimated by assuming that the hoop stress at the edge of the breakout is exactly equal to the UCS. Thus, knowing the rock parameters, minimum horizontal stress (e.g. from hydraulic fracturing or leak-off tests), and measuring breakout width from borehole caliper or imaging logs, one can estimate the maximum horizontal stress (Barton et al. 1988). However, the accuracy of stress estimation relies on the uncertain parameter of breakout width, so the resulting confidence interval can be quite wide. Dynamic failure process is complicated and often determined by structural heterogeneity resulting in variable breakout width within one rock layer. In addition, when the rock strength is



higher than the in situ circumferential stress, the failure does not occur which limits the information available to constrain stress. In such conditions, the circumferential stress can be increased by heating the borehole wall, leading to development of thermally induced breakouts.

Previously, borehole tests in underground research laboratories proved the ability of the borehole heating method to induce breakouts thermally in the  $\sigma_h$  direction (Hakami and Christiansson 2011; Siren et al. 2015; Voegeli et al. 2020; Nopola et al. 2020). In the present study, we validated the method experimentally using a true-triaxial apparatus with acoustic emission monitoring in order to assess its potential to estimate the maximum horizontal stress magnitude. During the tests, we first constrained the room-temperature borehole strength. Then, in elevated-temperature tests, we loaded the samples mechanically within the elastic range, and later added additional compression thermally by heating the borehole walls. The onset of breakout development was identified using acoustic emission events and related to the applied far-field stress through analysis of thermoelastic stresses.

The manuscript is organized as follows. First, theoretical background regarding thermoelastic stress around borehole and the strength of borehole wall is briefly presented in Sect. 2. Next, in Sects. 3, 4 and 5 we describe the laboratory work: used rock samples, experimental methods and data analysis, respectively. Finally, Sect. 6 provides description and discussion of the thermal breakout method for maximum horizontal stress estimation.

## 2 Theoretical Background

# 2.1 Stress Around Borehole

For simplicity, throughout the paper we restrict the analysis to a vertical borehole situation, where the weight of overburden is one of the principal stresses, and the other two are horizontal. Stresses around boreholes of arbitrary orientation have been analyzed by Peška and Zoback (1995). We also disregard effects related to anisotropy.

In his classical paper, Kirsch (1898) described stress concentration around an opening in a plate loaded by far field uniaxial stress, which has been further generalized to two dimensions by superposition. According to Kirsch's solution, and assuming plane strain condition in the horizontal plane, the effective principal stresses at the borehole wall are equal to (e.g Zoback 2007; Fjær et al. 2008):

$$\begin{split} \sigma_{rr} &= \frac{1}{2} (\sigma_{\rm H} + \sigma_{\rm h}) \left[ 1 - \frac{a^2}{r^2} \right] \\ &+ \frac{1}{2} (\sigma_{\rm H} - \sigma_{\rm h}) \left[ 1 - \frac{4a^2}{r^2} + \frac{3a^4}{r^4} \right] \cos 2\theta + \frac{\Delta P a^2}{r^2}, \end{split} \tag{1}$$

$$\sigma_{\theta\theta} = \frac{1}{2} (\sigma_{\rm H} + \sigma_{\rm h}) \left[ 1 + \frac{a^2}{r^2} \right] - \frac{1}{2} (\sigma_{\rm H} - \sigma_{\rm h}) \left[ 1 + \frac{3a^4}{r^4} \right] \cos 2\theta - \frac{\Delta P a^2}{r^2}, \tag{2}$$

$$\sigma_{zz} = \sigma_{v} - 2\nu(\sigma_{H} - \sigma_{h}) \frac{a^{2}}{r^{2}} \cos 2\theta, \tag{3}$$

where  $\sigma_{\rm H}$ ,  $\sigma_{\rm h}$  and  $\sigma_{\rm v}$  are maximum horizontal, minimum horizontal and vertical effective stresses,  $\Delta P$  is the difference between in situ pore pressure and mud pressure, a is the borehole diameter, r is the distance from the center of the borehole,  $\theta$  is the angle from the direction of  $\sigma_{\rm H}$ , and v is Poisson's ratio. At the  $\theta$  azimuth of 90° ( $\sigma_{\rm h}$  or the breakout azimuth), where the hoop stress is most compressive, and assuming no difference between the mud and pore pressures, the principal stresses at the borehole wall become:

$$\sigma_{\theta\theta} = 3\sigma_{\rm H} - \sigma_{\rm h},\tag{4}$$

$$\sigma_{rr} = 0, (5)$$

$$\sigma_{zz} = \sigma_{v} + 2\nu(\sigma_{H} - \sigma_{h}). \tag{6}$$

In most cases, the hoop stress  $\sigma_{\theta\theta}$  is the largest principal stress, the axial stress  $\sigma_{zz}$  is the intermediate, and the radial stress  $\sigma_{rr}$  is the least principal stress. In the case of a vertical borehole,  $\sigma_{zz}$  can be the largest only in normal stress regime, with low horizontal stress magnitudes relative to  $\sigma_v$ . In the laboratory testing, we did not analyze such stress setting. Therefore, for the remainder of the paper, we assume that at the borehole wall in the azimuth of breakout, the principal stresses are:  $\sigma_1 = \sigma_{\theta\theta}$ ,  $\sigma_2 = \sigma_{zz}$ , and  $\sigma_3 = \sigma_{rr}$ .

It is also important to note that the axial stress  $\sigma_{zz}$  is not equal to the weight of overburden. Because of the assumption of plane strain (removal of borehole material does not induce vertical deformation of the surrounding area and therefore  $\varepsilon_{zz}=0$ ), the axial stress at the azimuth of breakout is equal to the overburden weight plus contribution from the horizontal stresses. From (6) we see, that for a Poisson's ratio equal to 0.25, the axial stress at the breakout azimuth is higher than  $\sigma_v$  by half of the horizontal stress difference. Therefore, in high horizontal stress difference settings, the axial stress at breakout azimuth can be significantly higher than  $\sigma_v$ .

## 2.2 Borehole Strength

Breakout failure is most commonly predicted using the Mohr–Coulomb criterion which can be described by the following relations (e.g. Zoback et al. 1985; Zoback 2007):



$$\sigma_1 = \text{UCS} + q\sigma_3, \quad q = \left(\sqrt{1 + \mu^2} + \mu\right)^2,$$
 (7)

where UCS is the uniaxial compressive strength and  $\mu$  is the coefficient of internal friction. The mud weight is usually chosen close to the pore pressure magnitude, and therefore the radial stress is close to zero. Thus, it is common to assume that the borehole wall is in uniaxial stress condition, the hoop stress being the only stress component contributing to breakout failure. In such case, the breakout is predicted when the hoop stress reaches the UCS. Two main shortcomings of this simple approach: the influence of the intermediate stress and size effect are discussed in Sect. 6.

In the remainder of the paper, we assume that borehole wall failure occurs when hoop stress reaches some critical value. Lin et al. (2020) used the term borehole wall strength (BWS) for the critical hoop stress at the onset of breakout. We choose to use borehole compressive strength (BCS) in this paper to further emphasize the compressive mode of breakout failure.

#### 2.3 Thermal Stress Around Borehole

When the borehole is heated, the rocks around it are forced to expand, but this expansion is constrained by the unheated rocks farther away from the borehole. Therefore, compressional stress is induced.

Thermal stresses around a borehole assuming linear thermoelasticity, material isotropy and plain strain conditions are calculated using: (Stephens and Voight 1982; Noda et al. 2003):

$$\sigma_{rr}^{T} = \frac{\alpha E}{1 - \nu} \frac{1}{r^{2}} \int_{a}^{r} \Delta T(r', t) r' dr',$$

$$\sigma_{\theta\theta}^{T} = -\frac{\alpha E}{1 - \nu} \frac{1}{r^{2}} \left[ \int_{a}^{r} \Delta T(r', t) r' dr' - \Delta T(r, t) r^{2} \right],$$

$$\sigma_{zz}^{T} = \frac{\alpha E}{1 - \nu} \Delta T(r, t),$$
(8)

where  $\alpha$  is the linear coefficient of thermal expansion, E is the Young's modulus, v is the Poisson's ratio, r is the radial distance from the center of the borehole, a is borehole radius and  $\Delta T$  is the function describing change of temperature with radial distance and time. From the above equations we see that at the borehole wall, the radial thermal stress vanishes and the thermal hoop and axial stresses are equal to:

$$\sigma_{\theta\theta}^T = \sigma_{zz}^T = \frac{\alpha E}{1 - \nu} \Delta T. \tag{9}$$



#### 3.1 Basic Information

For laboratory testing, we chose two rock types with different properties: high-porosity and low-strength Berea sandstone, and low porosity and high strength Niagaran dolomite. Both rocks are homogeneous and isotropic. The reason for such choice was to check how the thermal breakout method works for two examples of rocks, significantly different in terms of porosity and strength.

Berea sandstone (late Devonian, river sand origin) samples are composed mainly of quartz, with minor amount of feldspars and carbonates. The used variety of Berea is characterized by high porosity of 22.5%, and density equal to  $2050 \text{ kg/m}^3$ .

Niagaran dolomite (Silurian–Niagaran series, reef dolomitic limestone) is composed of dolomite, calcite, with minor amount of quartz. It is a massive, vug-free, homogeneous rock. The variety used in the study is characterized by 4% porosity, and density equal to 2720 kg/m<sup>3</sup>.

# 3.2 Strength in Triaxial Compression

The samples for conventional, triaxial compression tests were 76.2 mm (3 in.) tall, 38.1 mm (1.5 in.) diameter. During the tests, samples were loaded at constant strain rate  $10^{-5}$ /s until failure, at various constant levels of confining pressure. Both axial and lateral deformations were measured during the tests. Figure 1 depicts the stress–strain data acquired during triaxial compression tests. Both rocks fail in brittle manner at low confining pressures and exhibit moderate ductility at higher confining pressures. The failure is preceded by change in volumetric strain from compressional to dilatant.

Table 1 presents the summary of triaxial compression test results. The average elastic parameters are: Young's modulus equal to 75 and 20 GPa, and Poisson's ratio equal to 0.25 and 0.19, for Niagaran dolomite and Berea sandstone, respectively. A uniaxial compressive strength of 259.3 MPa was measured for the Niagaran dolomite, while the Berea sandstone exhibited UCS equal to 59.9 MPa.

# 3.3 Thermal Properties

Thermal property testing consisted of thermal expansion tests on cylindrical samples, and thermal conductivity and thermal diffusivity tests on disk samples.



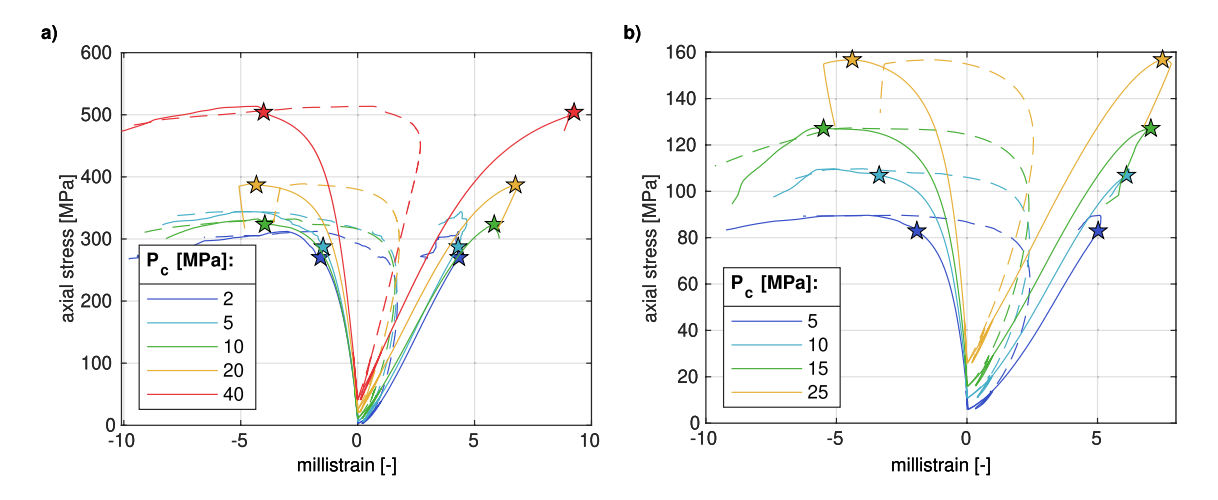


Fig. 1 Triaxial compression data acquired for a Niagaran dolomite, and b Berea sandstone. Solid lines present the axial and radial strain, and the dashed lines present the volumetric strain; stars indicate the moment of failure

Thermal expansion was measured using a cylindrical sample equipped with LVDTs (linear variable differential transducers) placed in a furnace. The sample was unconfined, i.e. tests were at atmospheric pressure, and only the axial expansion was recorded by the LVDTs. The thermal expansion data are presented in Fig. 2, and the coefficients are equal to  $1.51 \cdot 10^{-5}$  and  $1.48 \cdot 10^{-5}$  strain per degree K, for Niagaran dolomite and Berea sandstone, respectively.

Thermal conductivity and diffusivity were measured during hot disk tests. In these tests a disk heater with a thermistor is placed between two finished samples prepared from the same core. Then, a pulse of heat is applied through the heating disk and heat diffusion is observed. The following parameter values were obtained: k = 2.2 W/(m K),  $C_p = 730$  J/(kg K) for the

Berea sandstone, and k = 4.2 W/(m K),  $C_p = 810 \text{ J/(kg K)}$  for Niagaran dolomite.

# 4 Experimental Methods

# 4.1 Sample Preparation for True-Triaxial Tests

Samples with dimension of  $139.7 \times 139.7 \times 203.2$  mm (5.5  $\times 5.5 \times 8$  inches) or  $139.7 \times 139.7 \times 152.4$  mm (5.5  $\times 5.5 \times 6$  in.) were cut from bigger blocks and ground to size on precision surface grinder, with faces parallel within 50  $\mu$ m. At the center of each block a 19.1 mm (0.75 in.) diameter borehole was predrilled. In addition, for elevated-temperature tests,

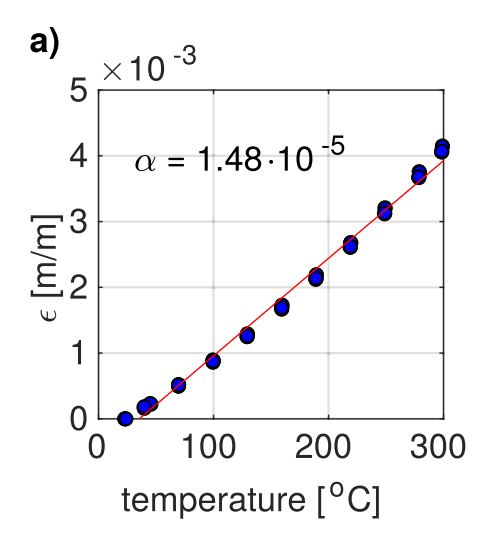
**Table 1** Summary of triaxial compression test results; Nia—Niagaran dolomite samples, Ber—Berea sandstone samples; E is the Young's modulus, v is the Poisson's ratio,  $\sigma_{axial}$  is the maximum axial stress at failure and  $P_c$  is the confining pressure at which the test was performed

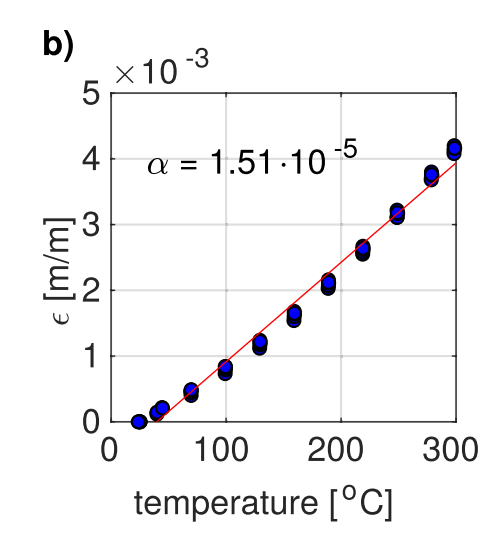
	with	<u> </u>		=
Sample	E (GPa)	ν (–)	$\sigma_{\rm axial}$ (MPa)	$P_{\rm c}$ (MPa)
Nia4	74.2	0.292	270.0	2
Nia6	75.9	0.284	287.4	5
Nia9	68.2	0.281	323.5	10
Nia11	72.2	0.226	387.0	20
Nia8	80.6	0.212	503.9	40
Ber1	_	_	52.3	0
Ber3	18.2	0.221	82.9	5
Ber5	19.1	0.191	106.9	10
Ber2	20.2	0.186	127.1	15
Ber4	21.5	0.156	156.8	25
	$E_{av}$ (GPa)	ν <sub>aν</sub> (–)	UCS (MPa)	μ (–)
Niagara	75	0.25	259.3	1.04
Berea	20	0.19	59.9	0.77

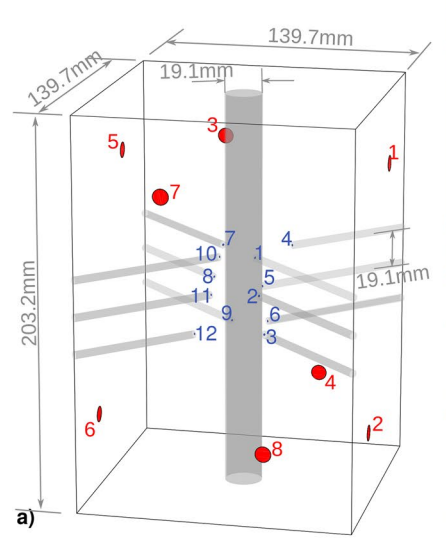
Lower part of the table provides average elastic parameters and Mohr–Coulomb failure parameters: UCS and internal friction coefficient  $\mu$ 

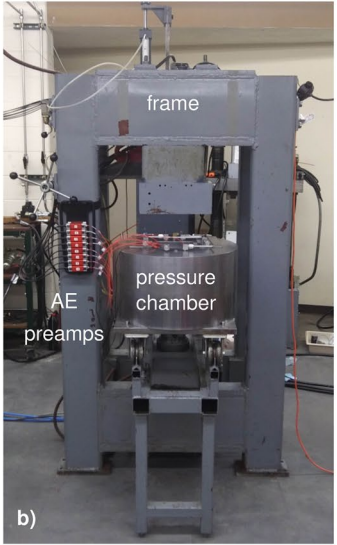


Fig. 2 Thermal expansion coefficient testing results; a Berea sandstone, b Niagaran dolomite; red line shows the linear fit of the strain measurements vs. temperature. The thermal expansion coefficient (the slope of the red line) for both rock types is approximately constant with temperature (color figure online)









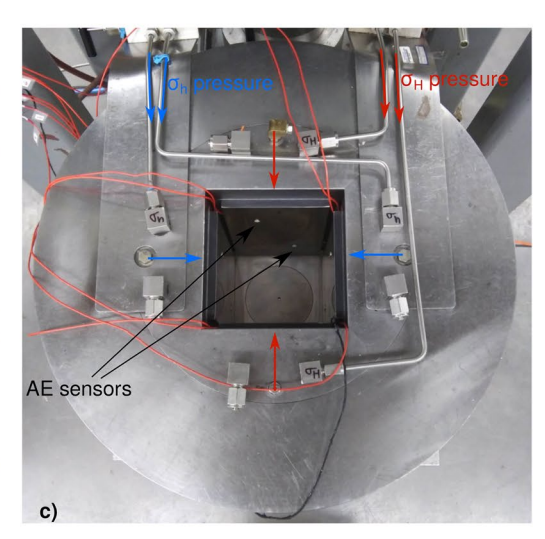


Fig. 3 a Sample dimensions and positions of acoustic emission sensors (red circles) and thermocouples (blue dots), b UW-Madison true-triaxial apparatus, c pressure chamber with acoustic emission sensors (color figure online)

twelve thermocouple holes were drilled from the corners of the sample. Sample schematic is depicted in Fig. 3a. The faces of the sample were covered with a thin layer of stearic acid mixed with vaseline (with equal weight fractions) to reduce friction between the rock and the pistons (Labuz and Bridell 1993).

## 4.2 True-Triaxial Test Setup

The true-triaxial apparatus used in the experiments was designed and built at the University of Wisconsin–Madison at the beginning of 1990s and recently modified to allow AE monitoring. Previous results obtained using this apparatus were published by e.g. Lee and Haimson (1993), Haimson

and Song (1993), Haimson and Kovacich (2003) and Haimson and Lee (2004).

The apparatus consists of a loading frame, which is used to apply the vertical stress, and a cylindrical chamber with two pairs of hydraulic pistons that are used to apply the horizontal stresses (Fig. 3b, c). The pistons are driven by two separate pressure intensifiers, which allows the independent application of the two orthogonal horizontal stresses. Each piston is equipped with two o-rings for positioning and sealing the cavities where pressure is applied. The forces acting on the sample faces are calculated from pressure in the cavity multiplied by piston surface. The o-ring friction reduces the applied force, and to exclude this effect, we conducted calibration tests: for the low-stress range, we used an external load



cell, and for intermediate- and high-stress range, we measured strains in an aluminum block with known elastic parameters.

We performed two types of true-triaxial experiments: room-temperature and elevated-temperature. The room-temperature tests were meant to constrain the borehole compressive strength (BCS), i.e. the hoop-stress level at which the breakout forms. Then, during elevated-temperature tests the samples were loaded mechanically below the BCS, and the additional compression needed to create a breakout was induced thermally.

We applied the following procedure for room-temperature tests: first, the hydraulic pistons and the loading frame were brought to contact with the rock sample. Then, all three principal stresses were increased simultaneously at a loading rate of 0.1 MPa/s to reach the intended minimum horizontal stress and vertical stress magnitudes. After reaching the assigned magnitudes for  $\sigma_h$  and  $\sigma_v$ , the maximum horizontal stress  $\sigma_H$ , was increased until the breakout formed at the same loading rate of 0.1 MPa/s. After breakout formation, the sample was unloaded, at 0.2 MPa/s. Stress data were logged at 0.5 s sampling intervals.

In elevated-temperature experiments, the first stages were similar, but then the maximum horizontal stress was increased to levels below the critical magnitude required to create a breakout (assessed from previous room-temperature tests). Additional compression necessary to induce compressive borehole wall failure was induced by heating the borehole. We used a cylindrical cartridge heater to heat the borehole wall (191 mm long, 12.7 mm diameter, Nichrome resistive wire inside Incoloy sheath, 1000 W).

#### 4.3 Acoustic Emission Data Acquisition

Piston faces were equipped with additional front plates where the acoustic emission sensors were installed (Fig. 3c). A disk of silicone was placed behind each sensor to apply constant coupling force between the sensor and the rock face. During the experiments, eight piezoelectric sensors recorded AE events. In addition, active pulsing was performed in 60 s intervals to measure P-wave velocities. The acquisition frequency spectrum of the sensors was 0.1–0.8 MHz, with maximum sensitivity between 0.2 and 0.3 MHz. Sensor positions are depicted in Fig. 3a. The data were recorded using an acoustic emission acquisition system with triggering set so that a signal over preset voltage threshold in any of the eight channels triggered acquisition in all channels. Therefore, each event consists of eight traces with identical start time and length. Sampling frequency was set to 10 MHz.

## 4.4 Borehole Camera Recording

During room-temperature true-triaxial tests we deployed a borehole camera inside the borehole at approximately two thirds of its height, to acquire video recordings of the borehole wall during formation and development of breakout structures.

## 4.5 Temperature Data Acquisition

During elevated-temperature tests, the temperature was measured by twelve K-type thermocouples installed in holes drilled from the edges (Fig. 3a). The thermocouples were installed at approximately 2, 5, 10 and 20 mm from the borehole wall at heights 82.6, 101.6 and 120.7 mm. Sampling interval was set to 1 s.

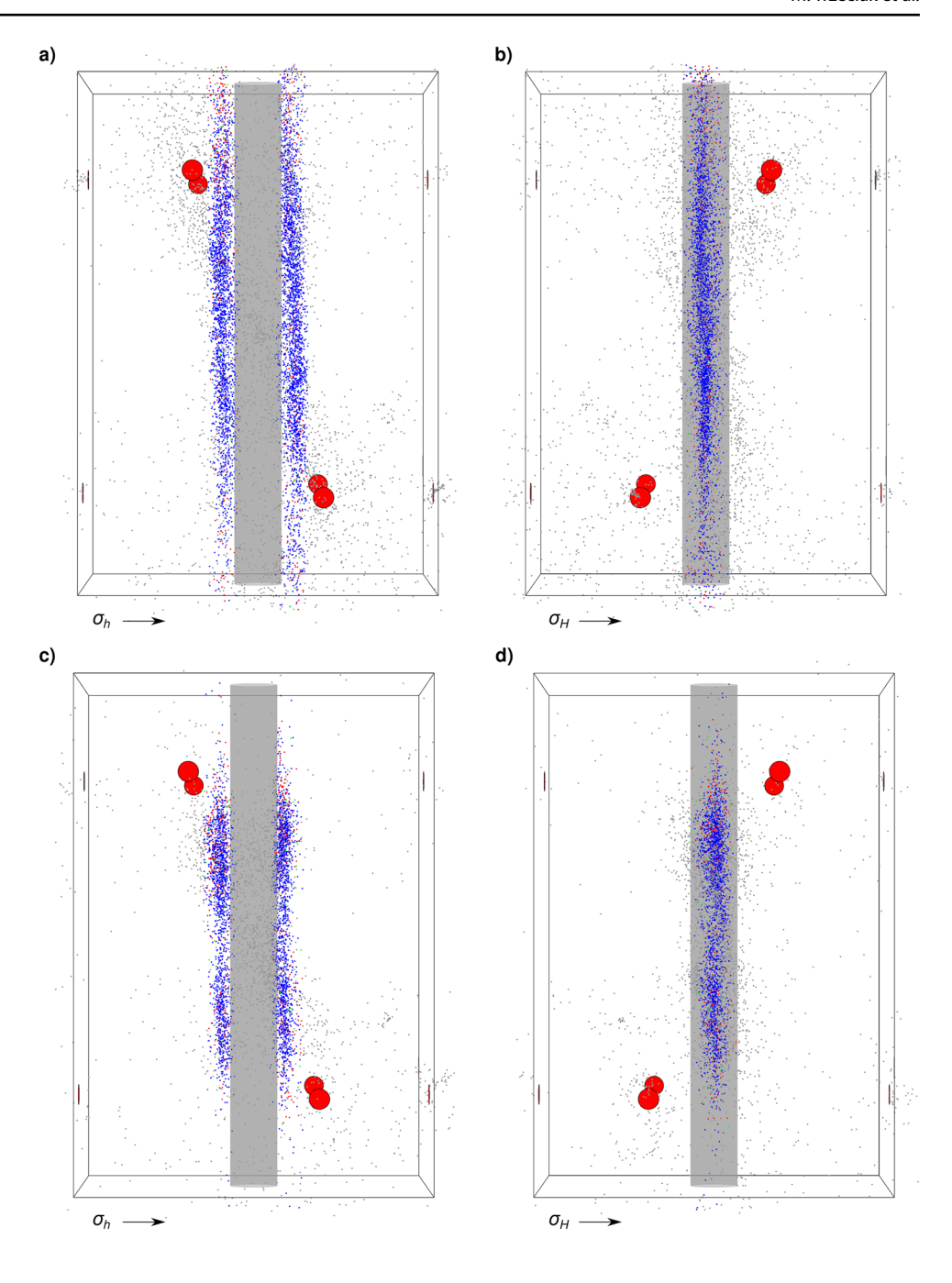
# 4.6 Stress Conditions in True-Triaxial Experiments

The principal stresses at the borehole wall are the hoop (circumferential) stress  $\sigma_{\theta\theta}$ , radial stress  $\sigma_{rr}$  which is the fluid pressure that acts at the wall, and  $\sigma_{zz}$  acting parallel to the borehole axis. In field scale boreholes,  $\sigma_{zz}$  varies azimuthally around the borehole according to (6) due to the plane strain assumption, i.e. the deformations are constrained along the borehole axis. We ran finite element and FLAC simulations to check the  $\sigma_{zz}$  distribution during a true-triaxial experiment where the block size is limited. Elastic finite element modeling assuming rigid pistons (uniform displacement along rock sample faces) showed plane strain  $\sigma_{zz}$  variation in the horizontal slices (perpendicular to borehole axis) and no variation along the height of the borehole. More detailed FLAC modeling, where pressure was applied to the back of steel pistons as in a real experiment, showed a small deformation of the pistons at the contact with the rock. This leads to some  $\sigma_{zz}$  variation along the height of the borehole. However, approximately at two borehole diameters into the borehole from the top and bottom faces, the azimuthal  $\sigma_{zz}$ variation follows the plane strain distribution.

In a dry borehole loaded with far-field stresses, at the azimuth of breakout according to Kirsch's solution, the hoop stress at the borehole wall equals  $\sigma_{\theta\theta}=3\sigma_H-\sigma_h$ . For the rock sample and borehole size used in our experiments (19.05 mm diameter, 139.7 mm side length), according to the finite element model with uniform displacement boundary conditions at all faces, the stress concentration factor is 3.07 instead of 3. Therefore, we assumed that the stresses applied at the pistons can be treated as far-field, because the stress concentration factor does not deviate significantly ( $\sim$  2%) from Kirsch's analytical result.

In uniaxial laboratory tests on rock cylinders the sample acquires a barrel shape because of friction at the top and bottom faces that constrains deformation. Even though we

Fig. 4 Acoustic emission location examples; blue dots-compressional events, red dots-shear events, green dots-tensile events; gray dots-events located outside the breakout zone. a Ber3 sample (room-temperature) located events in the plane of minimum horizontal stress, b Ber3 sample (room-temperature) located events in the plane of maximum horizontal stress, c Ber5 sample (heated) located events in the plane of minimum horizontal stress, d Ber5 sample (heated) located events in the plane of maximum horizontal stress (color figure online)



apply friction reducer to the piston faces (Labuz and Bridell 1993), a similar phenomenon may still be present in the true-triaxial tests especially when  $\sigma_H$  is raised far above  $\sigma_h$  and  $\sigma_v$  during the final loading stage in our experiments. Therefore, we modeled numerically an endmember case: uniaxial  $\sigma_H$  loading assuming infinite friction at the pistons, to check how it influences the vertical stress distribution at the borehole wall. The modeling showed that even at  $\sigma_H$  equal to 100 MPa, the magnitude of additional  $\sigma_{zz}$  induced by friction in the direction of breakout, was less that 10 MPa. We hypothesize that in our experiments, with the use of friction reducer and where block barreling is constrained by other pistons,

this number decreases to a maximum of a few percent of the applied horizontal stress.

# 5 Experimental Data Analysis

Gathered experimental data consists of triaxial compression results, thermal properties (both presented in Sect. 3), and acoustic emission data, stresses measured during the true-triaxial tests, borehole video recordings (for room-temperature tests) and temperature measurements (for elevated temperature tests). First, we present the acoustic emission



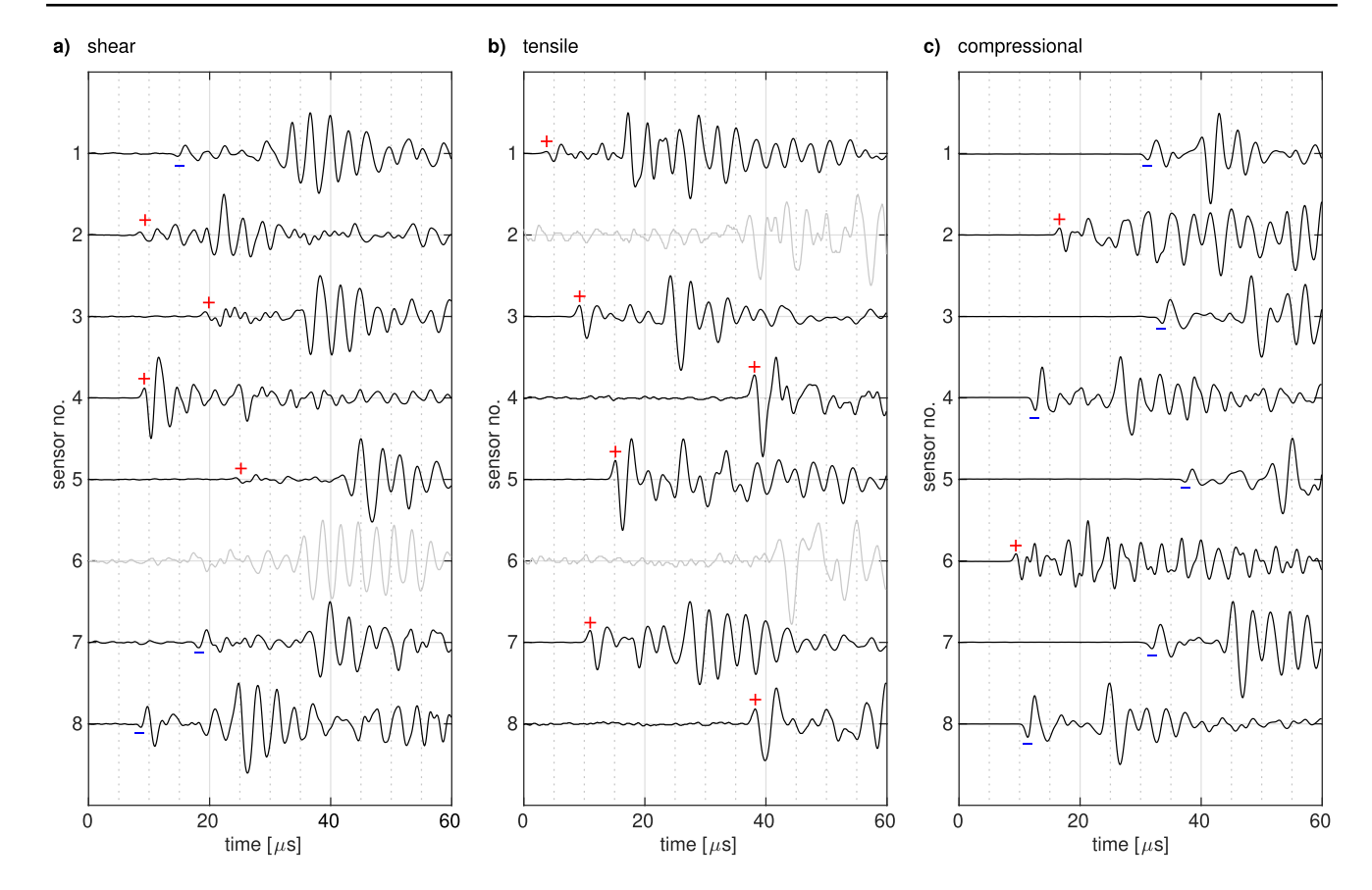


**Fig. 5** Example acoustic emission events and polarity analysis; **a** seven sensors recorded good quality arrivals, four positive and 3 negative, average polarity is equal to 0.143, event classified as shear, **b** six sensors recorded good quality arrivals, all positive, the average polarity equals 1, event classified as tensional,  $\mathbf{c}$  eight sensors

recorded good quality arrivals, two positive and six negative, average polarity equals – 0.5, event classified as compressional. Gray waveforms excluded from the polarity analysis because of insufficient quality

data analysis used to constrain the moment of breakout initiation and temperature extrapolation to the borehole wall. Next, we analyze the obtained data for Berea sandstone and Niagaran dolomite samples.

# 5.1 Acoustic Emission Data Analysis

Acoustic emission data processing consisted of three main steps: (1) locating the events, (2) selecting events related to breakout formation (close to the borehole wall at the azimuth of minimum horizontal stress), and (3) calculating the released acoustic emission energy and deformation modes for selected events.

First arrival picking was done automatically using the Akaike Information Criterion (AIC) based autopicker (Akaike 1974), implemented in Matlab by Kalkan (2016). Pick quality was ensured by (1) checking the linearity of the AIC function for the waveform data before the picked first arrival with a threshold  $R^2$  fit quality equal to 0.97, and (2) by finding the first motion amplitude, calculating the signal to noise ratio, and taking only waveforms with s/n ratio

higher than 8. Location was performed by minimizing the L1 norm of traveltime residuals using the simplex method (Nelder and Mead 1965).

Next, we selected the events within the zone of breakout development at the azimuth  $\pm 30^{\circ}$  from the azimuth of  $\sigma_h$ , at distances from 0 to 7.5 mm from the borehole wall, at both sides of the borehole. Example of locations for room-temperature and heated experiments are presented in Fig. 4.

For the selected breakout events, we calculated the cumulative number of events, cumulative energy, and for good quality recordings we also distinguished whether the event was compressional, shear or tensile by analysis of first motion polarity (Zang et al. 1998). Number of sensors and the geometry of the experiment did not allow to perform moment tensor inversion reliably. However, the polarity method allows to describe qualitatively the source mechanism and gives comparable results to moment tensor inversion (Graham et al. 2010). In our system, negative polarity indicates material compression, and positive



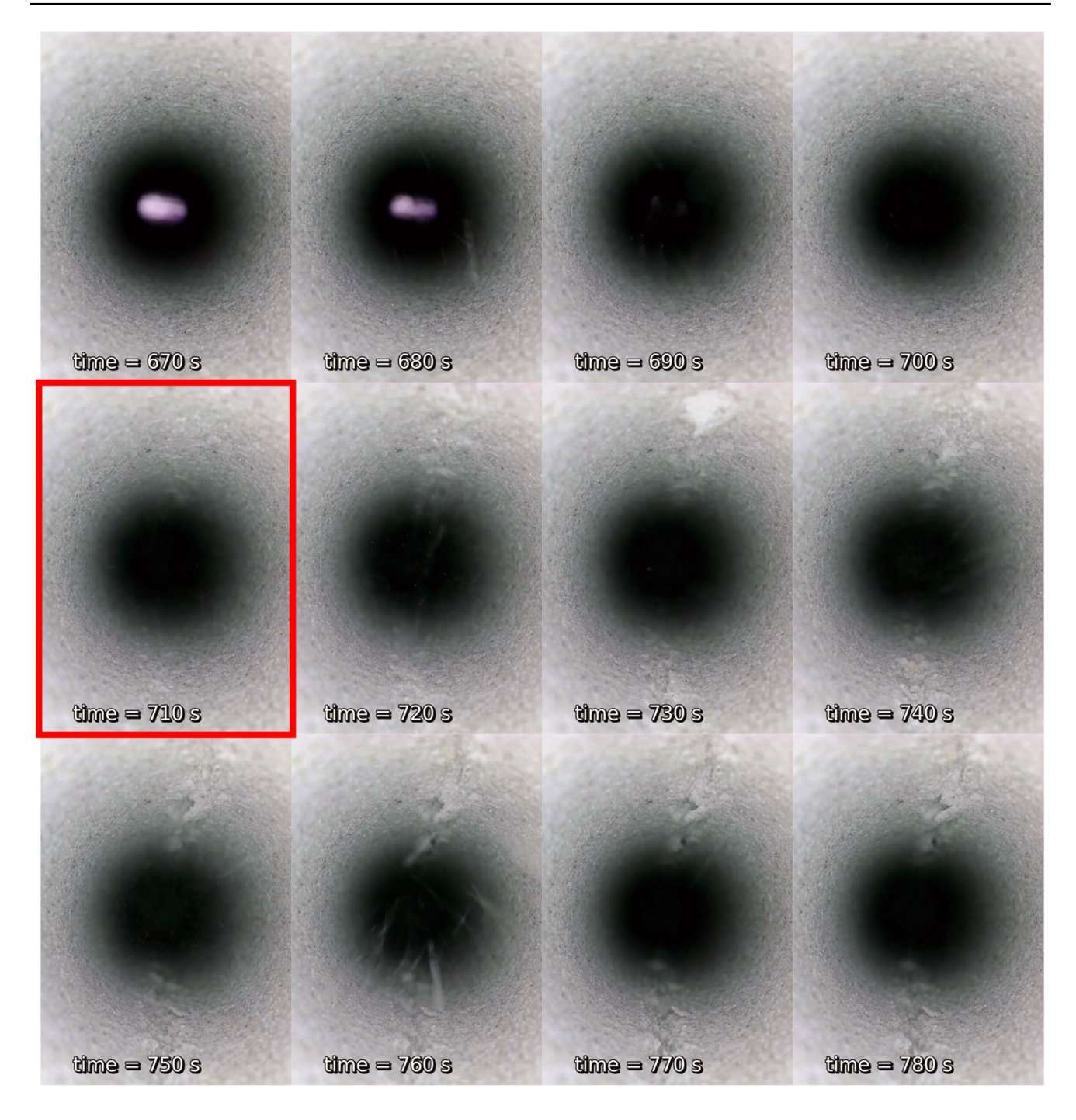


**Fig. 6** Snapshots of the borehole camera recording for Ber3 sample. Videos for Ber3 and Ber6 samples available in supplementary materials. The highlighted frame is the time when the AE events begin as shown in Fig. 7 (Ber3)

polarity extension. Thus, for events with at least six properly assessed polarities, we calculated the average polarity:

$$pol = \frac{1}{k} \sum_{i=1}^{k} sign(A_i),$$
 (10)

where  $A_i$  is the amplitude of first motion at *i*th sensor. Finally, we classified the events assuming that the polarity is below -0.25 for compressional events (*C*), is between -0.25 and 0.25 for shear (*S*), and is higher than 0.25 for tensile events (*T*). Figure 5 presents examples of the waveforms and polarity analysis.



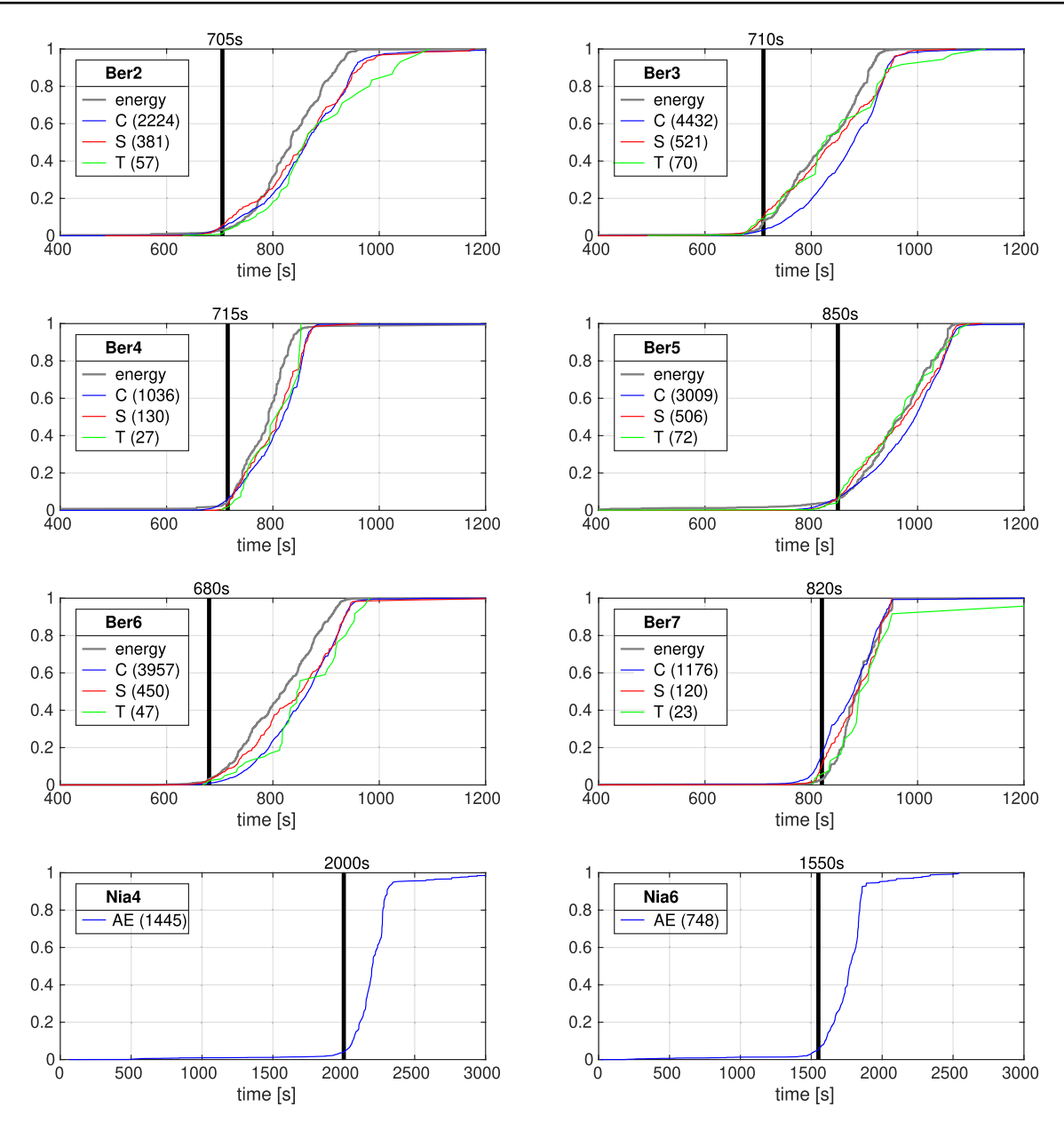


Fig. 7 Onset of breakout determination for the Berea sandstone samples. The curves show cumulative acoustic emission pseudo-energy (amplitude of first arrival squared), cumulative count of compressional (C) events, cumulative count of shear (S) events, and cumulative count of tensile (T) events. All curves are normalized and the

vertical axis represents the fraction of emitted energy or overall number of events. The black line and timestamp indicates the picked onset of breakout—hoop stress at this picked time is used as BCS in subsequent calculations

## 5.2 Onset of Breakout Determination

The moment of breakout initiation was investigated using acoustic emission signals and, for the room-temperature tests, using the borehole wall video recordings.

The video images were first compared to acoustic emission characteristics to establish a method for picking the onset of breakout. The visible failure on the borehole wall appeared a moment after tensile and shear events started to appear, and the AE energy rate increased. We did not record

video for heated tests because the borehole was occupied by heater element. However, since the AE characteristics were similar to room-temperature tests, we were able to constrain the onset of breakout based on the onset of tensile and shear events as well as the onset of AE energy rate increase. Snapshots of the video captured for Ber3 are presented in Fig. 6. The overview of AE based breakout picking is presented in Fig. 7. For the Berea sandstone samples, the number of recorded events was large and allowed us to constrain the polarities and the released energy. For Niagaran dolomite



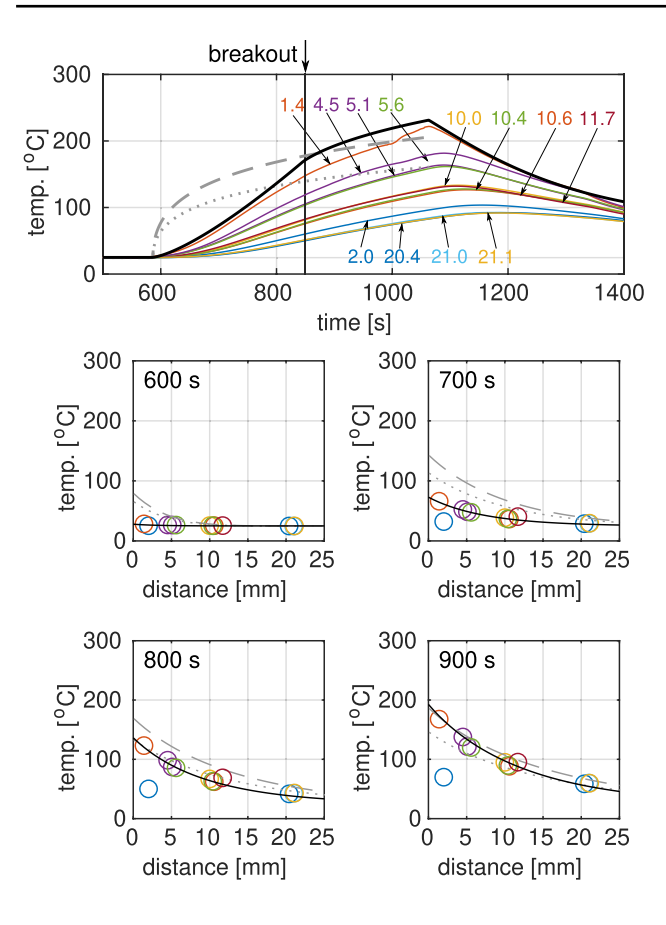
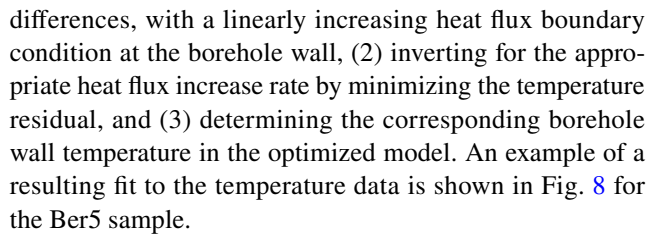


**Fig. 8** Thermocouple measurement extrapolation to the borehole wall, example from Ber5 sample. Colored curves show the thermocouple measurements, the black line shows the borehole wall extrapolation. The numbers with arrows indicate distance of each thermocouple from the borehole wall. Bottom subplots show snapshots of temperature distribution as a function of distance from the borehole wall. Gray dashed and dotted lines indicate examples of data fits using constant heat flux with two different magnitudes (at the top subplot showing the borehole wall extrapolation); regardless of the applied magnitude, this model does not fit the experimental dataset (color figure online)

samples the number of events were relatively small, and polarity analysis was not possible. Therefore, breakout onset picking was done based only on the cumulative count of all events within the breakout zone.

# 5.3 Thermal Stress Calculation

To calculate the thermally induced borehole stresses during the heated experiments, information on the borehole wall temperature is needed (Eq. 9). Because direct measurement of the borehole wall temperature is difficult, we estimated the borehole wall temperature by extrapolating the rock temperature measured by the array of thermocouples at several distances from the borehole wall. This was done by: (1) calculating the radial temperature profile using a radially symmetric heat conduction model, discretized using finite



Because a constant voltage was supplied to the heater during the experiment, we first considered using a constant heat flux boundary condition at the borehole wall to fit the temperature data. However, such boundary condition does not reproduce the qualitative features of the temperature data. As indicated by the gray dashed and dotted curves in Fig. 8, the concavity of the predicted temperature rise does not match the data. As a result, the constant flux model overestimates the temperature rise initially, but later underestimates the rock temperature.

The heat flux increased with time most likely due to increased thermal radiation. Because the heater was not in contact with the borehole wall (there was an approximately 3 mm gap), conduction and radiation were the dominant mechanisms of heat transfer. Ignoring convection, heat conduction through air is proportional to the temperature difference between the heater and the borehole wall. Radiation heat flux is proportional to the temperature difference raised to the power of 4 according to the Planck's law. Therefore, as the Incoloy sheath temperature increased faster than the borehole wall temperature, heat transfer rate also increased over time. The exact trend of how the heat flux increases over time is difficult to constrain as it involves various nonlinear factors such as, increase in resistance of the Nichrome heater element with temperature, convection of the air between the heater and the rock, heat transfer between the Nichrome heater element and the Incoloy sheath. However, a linearly increasing heat flux is a more plausible boundary condition than a constant heat flux model. Figure 8 also shows that the increasing heat flux model fits the data remarkably well up to 900 seconds, which is well after the onset of breakout formation.

The borehole wall temperature was used to calculate the thermal stress using Eq. (9), using average elastic parameters presented in Table 1, and linear thermal expansion coefficient equal to  $1.48 \cdot 10^{-5} \varepsilon/\mathrm{K}$  for Berea sandstone, and  $1.51 \cdot 10^{-5} \varepsilon/\mathrm{K}$  for Niagaran dolomite. The magnitude of induced thermal stress was equal to 0.4 and 1.4 MPa per degree Celsius, for Berea sandstone and Niagaran dolomite, respectively.

## 5.4 True-Triaxial Experimental Data Overview

The analyzed data set consists of four pairs of room- and elevated-temperature tests at the same minimum horizontal stress and vertical stress values: three Berea sandstone



**Table 2** Overview of truetriaxial breakout experiments; all stress magnitudes in MPa, temperature change  $\Delta T$  in  $^{\circ}$ C

Sample	$\sigma_{ m H}$	$\sigma_{ m h}$	$\sigma_{ m v}$	$\sigma_{\theta\theta}$ (BCS)	$\sigma_{zz}$	$\Delta T$
Ber2	47.0	10.3	10.3	130.7	24.2	0.0
Ber5	26.0	10.3	11.0	121.2	70.5	146.3
Ber3	53.4	20.3	20.0	139.9	32.6	0.0
Ber7	35.3	18.0	20.0	127.2	65.7	107.1
Ber6	50.5	20.3	10.0	131.3	21.5	0.0
Ber4	31.3	20.3	10.0	112.2	52.8	105.7
Nia4	141.5	10.3	10.0	414.4	75.6	0.0
Nia6	87.9	10.0	10.0	531.6	326.9	184.1

The UCS measured in triaxial compression tests was equal to 259.3 and 59.9 MPa, for Niagaran dolomite and Berea sandstone, respectively

sample pairs, and one Niagaran dolomite pair. An overview of the experiments is given in Table 2.

# 5.4.1 Berea Sandstone Samples

Clear breakout structures developed in all tested samples along the entire length of the borehole wall at the azimuth of minimum horizontal stress. Granular and porous structure of the rock promoted slip and grain rearrangement, resulting in high number of recorded AE events.

In the room-temperature tests the breakout developed at hoop stress (BCS) equal to 130.7, 139.9 and 131.3 MPa, for Ber2, Ber3 and Ber6 samples, respectively. It corresponds to respective BCS to UCS ratios equal to 2.2, 2.3 and 2.2. In elevated-temperature tests the breakout developed at hoop stress equal to 121.2, 127.2, and 112.2 MPa, for Ber5, Ber7, and Ber4 samples, respectively, resulting in BCS/UCS equal to 2.0, 2.1 and 1.9. Thus, in general the thermal breakouts seem to develop at a slightly lower circumferential stress compared to room-temperature breakouts. It suggests that the axial (intermediate) stress  $\sigma_{zz}$  does not have a large strengthening effect. However, the uncertainty of thermal stress estimation does not allow for definitive statements.

# 5.4.2 Niagaran Dolomite Samples

Because of the very high strength, Niagaran dolomite samples did not develop clear breakout structures along the entire borehole height for any of the samples. Breakouts were either very shallow, or developed on short intervals of the borehole height. Here, we report results from the two experiments out of eight that gave the best results. The room-temperature experiments were performed on shorter samples (152.4 mm, 6 in.) compared to heated experiments (203.2 mm, 8 in.) to achieve higher horizontal stress magnitudes. The number of recorded acoustic emission events was small compared to tests on Berea sandstone.

In the room-temperature Nia4 test the breakout formed at hoop stress (BCS)  $\sigma_{\theta\theta}$  of 414.4 MPa, while in the heated Nia6

experiment breakout was observed at  $\sigma_{\theta\theta}$  equal to 531.6 MPa. Such big discrepancy may be explained by the fact that in room-temperature test, the breakout only developed close to the top surface of the block and edge effects promoted failure. In addition, rock strengthening might have occurred due to the significant increase in the intermediate stress—the axial stress  $\sigma_{zz}$ . Note that in the heated dolomite test, the final axial stress  $\sigma_{zz}$  was about 250 MPa greater than the room temperature test, which is about 60% of the BCS value of 414.4 MPa recovered from the Nia4 test. On the other hand, for the Berea sandstone tests, the final axial stresses were about 30-45 MPa greater than the room temperature tests, which is only about 25–35% of the BCS of the Berea sandstones (Table 2). Therefore, we expect that the strengthening effect was more pronounced in the heated dolomite experiments, although we do not deal with the effect of the intermediate principal stress on rock strength in this study for simplicity. The resulting BCS to UCS ratios were equal to 1.6 and 2.1, for Nia4 and Nia6, respectively.

## 6 Discussion

The development and validation of the thermal breakout method for maximum horizontal stress estimation requires a careful examination of the appropriate rock strength criteria and any size effects on rock strength.

In the following subsections, we first review some selected polyaxial strength criteria which may be used in borehole strength assessments. We then discuss size effects of borehole strength seen in laboratory experiments. Next, we derive the thermal breakout equation and discuss sources of errors in the stress estimation. In the last subsection, we briefly address the field application of the method.



## 6.1 Polyaxial Strength Criteria

As was pointed out in Sect. 2.2 the simple Mohr-Coulomb criterion is most commonly used in borehole strength prediction. In this approach, the strength depends on the minimum and maximum principal stresses only. However, it is wellknown in the literature that the intermediate stress can have a significant influence on the strength of rock specimens (e.g. Mogi 1971; Haimson and Chang 2000; Chang and Haimson 2000; Ingraham et al. 2013; Ma and Haimson 2016; Lee and Haimson 2011). In polyaxial experiments, peak strength  $\sigma_1$  is obtained as a function of  $\sigma_2$  for various constant levels of  $\sigma_3$ . The experimental protocol starts with a conventional triaxial compression stress state of  $\sigma_1 > \sigma_2 = \sigma_3$ . The peak value of  $\sigma_1$  increases with increasing  $\sigma_2$ , reaches a maximum, and then decreases as the stress state approaches a conventional triaxial extension stress state of  $\sigma_1 = \sigma_2 > \sigma_3$ . A detailed description of various polyaxial strength criteria is outside the scope of the present work and only a few of them will be briefly presented.

Nadai (1950) proposed a general form of a criterion where the critical shear octahedral stress  $\tau_{\rm oct}$  is a function of the normal octahedral stress  $\sigma_{\rm oct}$ :

$$\tau_{\text{oct}} = f(\sigma_{\text{oct}}),\tag{11}$$

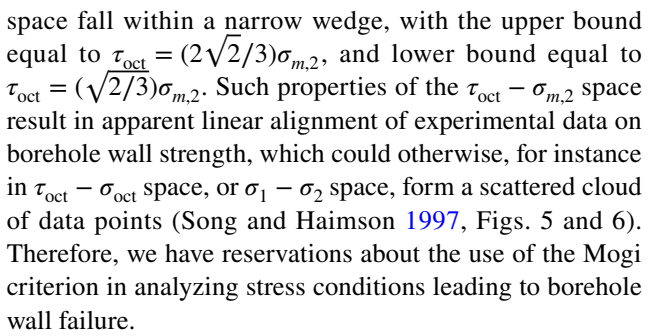
where

$$\begin{split} \tau_{\rm oct} &= \frac{1}{3} \sqrt{(\sigma_1 - \sigma_3)^2 + (\sigma_1 - \sigma_2)^2 + (\sigma_2 - \sigma_3)^2}, \\ \sigma_{\rm oct} &= \frac{1}{3} (\sigma_1 + \sigma_2 + \sigma_3). \end{split}$$

If one takes a linear relation between these quantities, the linear Nadai criterion is equivalent to the one developed by Drucker and Prager (1952). In this criterion the failure surface is a circle on the deviatoric plane, and therefore it overestimates the influence of  $\sigma_2$ , and can be suitable for pressure dependent ductile materials, and not brittle rocks. Mogi (1971) observed that his true-triaxial strength results are much better aligned when plotted in  $\tau_{\rm oct} - \sigma_{m,2}$  space rather than in  $\tau_{\rm oct} - \sigma_{\rm oct}$  space. Here  $\sigma_{m,2}$  is called the mean effective stress (Al-Ajmi and Zimmerman 2005) and it is given by:

$$\sigma_{m,2} = \frac{\sigma_1 + \sigma_3}{2}.\tag{12}$$

It is important to note, however, that  $\sigma_{m,2}$  is an empirical parameter and the Mogi criterion can give non-physical predictions where the  $\sigma_1 = f(\sigma_2)$  relation is non-unique and as a consequence, unloading may lead to failure (Ma and Ingraham 2018). Furthermore, if we restrict the analysis to polyaxial states with  $\sigma_3 = 0$  as is common for the borehole wall example, all the possible stress states in the  $\tau_{\rm oct} - \sigma_{m,2}$ 



Different failure criterion, commonly referred to as the modified Wiebols–Cook, has been proposed by Zhou (1994), and used in breakout analysis by Chang et al. (2010). The derivation and formulas can be found in the original paper, and here we focus on the main properties only. The modified Wiebols–Cook criterion is calibrated with Mohr–Coulomb so that the results from compression and extension tests and its corresponding parameters are used in the polyaxial strength estimation. Therefore, it is assumed that:

$$\sigma_1 = C_0 + q\sigma_3$$
 conventional triaxial compression,  
 $\sigma_1 = C_1 + q\sigma_3$  conventional triaxial extension, (13)

where  $C_0$  is the UCS,  $C_1$  is the strength at  $\sigma_1 = \sigma_2$ ,  $\sigma_3 = 0$ , and q is given by (7). The intermediate polyaxial strength between compression and extension at constant level of  $\sigma_3$  is a quadratic function of  $\sigma_2$ . The parameter  $C_1$  is crucial for correct strength assessment, but it is not commonly measured. Chang et al. (2010) assumed that  $C_1$  is a function of UCS and coefficient of internal friction. The polyaxial experimental data suggest, however, that  $C_1$  can be either higher, lower or similar to UCS, and it is difficult to propose a universal relation from the limited data available in the literature.

A modified Lade criterion was proposed by Ewy (1999), following a similar approach of matching Mohr–Coulomb parameters with a polyaxial strength criterion developed by Lade and Duncan (1975). However, as with the modified Wiebols–Cook criterion, it is not possible to reliably constrain the criterion using only conventional triaxial compression strength results.

The brief survey of polyaxial strength data and failure criteria shows that the intermediate stress has an important influence on strength, and that there are several formulations to account for that effect. It is impractical however, to run laborious true-triaxial strength tests for each engineering problem. Therefore, it is important to provide a method that can relate conventional strength properties derived from tests on cylindrical samples and polyaxial strength properties. The above mentioned criteria, modified Wiebols—Cook and modified Lade, attempt to provide such link, but require the use of assumptions that do not hold universally. We conclude, therefore, that the conventional triaxial compression



strength results are not enough to reliably constrain the parameters used in these polyaxial criteria.

Detailed, true-triaxial strength results are not available for Berea sandstone and the Niagaran dolomite tested in our experiments. Therefore, the assessment of intermediate stress influence on the ultimate strength of these rocks is only speculative. The results presented by Ma and Ingraham (2018) for high porosity sandstones similar to Berea sandstone, suggest that the influence of  $\sigma_2$  on strength is mild, especially when  $\sigma_2$  is below 50% of ultimate strength ( $\sigma_1$ ). Mogi (1971) presented results from true-triaxial testing of Dunham dolomite, which is characterized by similar UCS to the Niagaran dolomite. However, only uniaxial compression result is available for stress condition with  $\sigma_3 = 0$ , thus the assessment of intermediate stress influence in borehole setting is not possible.

## 6.2 Size and Stress Gradient Effects

According to Mohr–Coulomb criterion and under zero radial stress  $\sigma_{rr}$ , a borehole breakout is predicted when  $\sigma_{\theta\theta}$  equals the BCS. In theory BCS should be equal to UCS measured during standard tests, but experimental results in the literature show significant size effect which can be described by the BCS to UCS ratio (Carter 1992; Martin et al. 1994; Cuss et al. 2003; Meier et al. 2013; Lin et al. 2020). For small diameter boreholes the BCS can be several times higher compared to the UCS. As the borehole size increases, the BCS approaches the UCS magnitude. However, large borehole sizes cannot be tested because of the capabilities of laboratory systems, and therefore, the size effect is present.

Nesetova and Lajtai (1973) explained size effect using the stress averaging concept. From Eqs. (1–3) we observe that high stress gradients are present around the borehole and one end of a developing shear fracture adjacent to the borehole is in different stress state compared to the other end farther away from the wall. According to Nesetova and Lajtai (1973) ductile grain rearrangement effectively averages the stress over the length of the fracture. This characteristic length t may be regarded as a material property specific for a certain rock type. Thus, when borehole diameter is (relatively) close to the characteristic length, stress averaging decreases the stress concentration at the wall and the effective hoop stress at the wall is the average of hoop stress at r = a (Eq. 2), and at r = a + t. Such explanation was in agreement with field and laboratory results presented by Martin et al. (1994).

The stress averaging explanation of the size effect states that the strength of the material is stable, but the effectively acting stress is lower for small boreholes in laboratory scale. An alternative explanation states the opposite: the strength of a small volume comparable to the REV (representative elementary volume) of rock is higher compared to large volume. Such scaling relation can arise from random distribution of critical

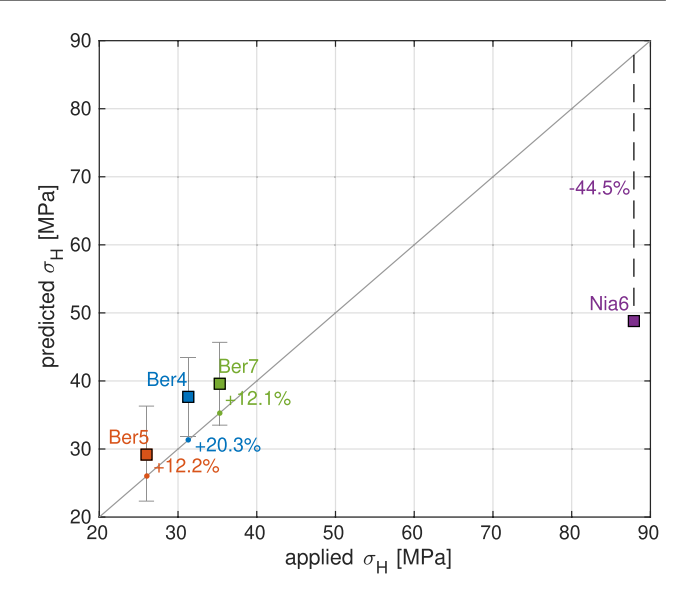


Fig. 9 Comparison of  $\sigma_{\rm H}$  applied during elevated-temperature experiments with predicted  $\sigma_{\rm H}$  calculated using (18)

flaws or unavailability of optimally oriented failure planes (e.g. Bažant 1999). Especially in porous, granular materials the failure is expected to happen along grain boundaries which are usually weaker than the grains themselves. Thus, if the region of high stress leading to failure does not contain high enough number of grain contacts the material appears stronger.

Stress gradient induced by heating the borehole wall can contribute to apparent strengthening of the borehole wall with a similar mechanism to the size effect as described by Nesetova and Lajtai (1973). When strong temperature gradients, and consequently strong stress gradients, are induced around the borehole, the length scale of the heated rock volume diminishes. This effectively leads to the reduction of size of the thermally stressed rock, leading to an apparent strengthening effect described above. Detailed experimental studies are necessary to address this issue in more detail.

In the current study, we did not analyze size effects nor the stress gradient effects of borehole wall strength. In our analysis, we used the same borehole diameter for all experiments, and used the measured BCS values directly to avoid size effects. Heating conditions were also kept consistent to avoid variability in results due to temperature gradients.

## 6.3 Thermal Breakout Method Derivation

The derivation of the thermal breakout equation for maximum horizontal stress for arbitrary failure criterion is straightforward. A general form of a failure criterion can be given as:

$$f(\sigma_1, \sigma_2, \sigma_3) = 0. \tag{14}$$



We assume that the failure starts at the point of maximum compression along the circumference (90° from the  $\sigma_H$  direction). Also, we assume that the hoop stress is the largest principal stress, the axial stress is intermediate, and radial is the least principal stress. In such case:

$$\begin{split} \sigma_1 &= 3\sigma_{\rm H} - \sigma_{\rm h} - 2P_0 + \frac{\alpha E}{1 - \nu} \Delta T, \\ \sigma_2 &= \sigma_{\rm v} + 2\nu(\sigma_{\rm H} - \sigma_{\rm h}) + \frac{\alpha E}{1 - \nu} \Delta T, \\ \sigma_3 &= \Delta P. \end{split} \tag{15}$$

To derive the thermal breakout equations for an arbitrary criterion, we simply insert (15) to (14) and solve for  $\sigma_H$ . As an example, we take the classical Drucker–Prager criterion which can be written as:

$$\tau_{\rm oct} = A + B\sigma_{\rm oct},\tag{16}$$

where A and B are criterion parameters. Next, we plug the principal stresses given by (15) in the definitions of  $\tau_{\rm oct}$  and  $\sigma_{\rm oct}$ , and solve for  $\sigma_{\rm H}$ . The calculation is straightforward, although results in a lengthy expression which is not necessary to explicitly present here. However, it is important to note that for the Drucker-Prager criterion, solving (16) for  $\sigma_{\rm H}$  results in two possible solutions and additional discussion is required to select the appropriate one. Similar non-uniqueness can be present in different polyaxial failure criteria as well.

If the Mohr–Coulomb criterion is used the thermal breakout formula to predict  $\sigma_H$  becomes simple and unique. Inserting (15) to (7) and rearranging gives:

$$\sigma_{\rm H} = \frac{1}{3} \left[ \text{UCS} + q\Delta P + \sigma_{\rm h} + 2P_0 - \frac{\alpha E}{1 - \nu} \Delta T \right]. \tag{17}$$

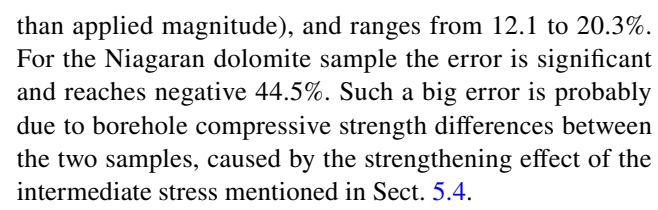
In our laboratory setting the rocks were tested in the absence of mud and pore fluids. Thus, Eq. (17) can be further simplified to:

$$\sigma_{\rm H} = \frac{1}{3} \left[ BCS + \sigma_{\rm h} - \frac{\alpha E}{1 - \nu} \Delta T \right],\tag{18}$$

where the uniaxial compressive strength (UCS) was substituted by the borehole compressive strength (BCS).

# 6.4 Laboratory Data Validation

For each heated sample, we calculated the predicted  $\sigma_H$  using Eq. (18) with the BCS measured in corresponding room-temperature test and compared the prediction with the  $\sigma_H$  magnitude applied during the experiment (Fig. 9). The comparison shows that for the Berea sandstone samples the prediction error for all samples is positive (higher prediction



In the case of Berea sandstone samples a standard error propagation analysis was carried out. Assuming 0.5 MPa error in  $\sigma_h$  and 10% error in the other parameters inserted to Eq. (18) the resulting prediction errors equal 6.9, 6.1 and 5.8 MPa, for Ber5, Ber7 and Ber4 samples, respectively (indicated by error bars in Fig. 9). Equation (18) consists of three terms: the BCS,  $\sigma_h$  and the thermal stress. Unit error in each of these terms propagates as 1/3 in the  $\sigma_H$  estimation. The minimum horizontal stress is always lower in magnitude compared to BCS and the elastic and thermal parameters can be accurately measured. Therefore, most of the  $\sigma_H$  prediction uncertainty lies in the BCS and borehole wall temperature measurement.

# 6.5 Other Sources of Uncertainty

Calculating the uncertainty of  $\sigma_H$  prediction is straightforward assuming Eq. (18) is correct, i.e. both the thermoelastic stress model, and Mohr–Coulomb failure criterion are appropriate for thermal breakout modeling. However, there are several other sources of uncertainty that require further evaluation.

The thermal breakout method is intended to be applied for stress environments that are not compressive enough to develop breakouts, which is caused by the lack of  $\sigma_{\rm H}$ magnitude in many situations. When heating occurs to induce breakouts, the stress state at the borehole wall is pushed closer to conventional triaxial extensional state  $(\sigma_1 = \sigma_2 > \sigma_3 = 0)$  because the thermal stress is added equally to both  $\sigma_{\theta\theta}$  and  $\sigma_{zz}$ . If wellbore failure occurs under such stress state, the  $C_1$  parameter (Eq. 13) may be a better estimate of the borehole strength rather than the  $C_0$  (=UCS). As was pointed out above, it is not straightforward to relate  $C_0$  and  $C_1$ , thus the sparsity of data on  $C_1$  poses a challenge. Note that this is different, for instance, when a breakout is induced by high  $\sigma_{\rm H}$  magnitude, because in this case,  $\sigma_{\theta\theta}$ increases three times faster than  $\sigma_{zz}$  (if Poisson's ratio is equal to 0.25) as  $\sigma_{\rm H}$  increases according to Eqs. (4) and (6). Thus the potential importance of constraining the  $C_1$  strength parameter is peculiar to the thermal breakout problem.

Furthermore, the Kirsch solution for stress around borehole is elastic, and does not take into acount any nonlinear plastic yielding that may occur prior to failure. However, this effect may be regarded as moderate as the stress calculation is based on the onset of breakout development in the proposed method.



The thermal stress calculation (9) includes the measured thermal expansion coefficient. The coefficient is calculated as the slope of linear fit to measurement data, but some degree of nonlinearity is usually present and introduces additional uncertainties. For instance, the measurements presented in Sect. 3.3 show that  $\alpha$  varies from  $1.0 \cdot 10^{-5} \ \epsilon/\mathrm{K}$  at room temperature to  $1.8 \cdot 10^{-5}$  $\varepsilon/K$  at 300°C for both rock types. We used the value of  $1.5 \cdot 10^{-5} \, \varepsilon/K$  corresponding to a linear fit to the entire temperature range in our thermal stress calculations. There are currently no definitive explanations for the cause of this nonlinearity, but some speculations include minerals expanding into crack volume at the beginning of the measurement or crack-opening that starts to occur later in the measurement. Note, however, that these thermal expansion measurements were performed with no confinement. Thus such nonlinear temperature effects may occur differently for rock constrained around a borehole. We therefore used an average value representing the whole temperature range for simplicity, but careful, detailed thermal expansion measurements are needed in future studies to evaluate the appropriate rock thermal expansion to use in calculating thermal stress.

Presented stress calculations rely on the radially symmetric heat transfer model with negligible conduction along the borehole axis. In the laboratory experiments, no axial heat transfer was observed. However, this effect may be present in borehole measurements, as heating takes usually much longer in the field compared to laboratory experiments (several hours compared to several minutes), and heat transfer along borehole axis can be more pronounced (Nopola et al. 2020). These are the factors that could affect the accuracy of the thermal breakout method that require careful examination in future studies.

Breakouts are zones of compressive failure of the borehole wall. However, the micromechanics of breakout deformation varies among different rock types (Haimson 2007). Therefore, it is important to provide links between standard rock strength tests and borehole strength for the specific rock under investigation.

# **6.6 Field Application**

Another important discussion is how the laboratory findings relate to in situ, field testing. In our project, a specialized borehole tool is under development and field testing is underway at the Sanford Underground Laboratory in South Dakota, United States. Several crucial elements of the field application need to be considered. First, because the borehole is filled with water or mud, radiation heating as in the laboratory will not be possible in the field. Thus the borehole tool is designed so that the heating pads

contact the rock directly to apply the thermal stress to the borehole wall. Borehole wall temperature measurement and inferring the thermal stress are the most challenging tasks in the field application of the method. Because thermocouples arrays similar to the ones in our laboratory test cannot be installed in the field, the borehole wall temperature needs to be measured at the borehole wall directly. This requires careful design of the tool so that the measurement is not affected by the heating pads. These could lead to additional uncertainties in the estimation of the maximum horizontal stress magnitude.

On the other hand, analysis in multiple boreholes drilled in various directions could give additional constraints on the maximum horizontal stress magnitude. Breakout orientations in boreholes misaligned with the principal stresses will vary depending on the magnitude ratios of the principal stresses according to the SFIB (stress and failure of inclined boreholes) equations (Peška and Zoback 1995). Such information could help mitagate additional uncertainties specific to field applications. The results and discussion of the field research will be presented in detail in a future paper.

#### 7 Conclusions

Laboratory work and data analysis showed that the thermal breakout method provides means to add important information about the in situ stress state. Similar to standard breakouts, the thermally induced breakouts form at the azimuth of minimum horizontal stress and allow to constrain the direction of maximum horizontal stress. Furthermore, if the onset of breakout is captured and the corresponding borehole temperature is measured, the thermal breakout equation allows to constrain the magnitude of the maximum horizontal stress. The equation requires as inputs the minimum horizontal stress, borehole strength, elastic constants, and thermal properties. Among these parameters the borehole strength is the most uncertain, as it is a value that quantifies the nonlinear process of rock failure and is also sensitive to rock heterogeneity and anisotropy. The current challenge is that a two-dimensional strength criterion (i.e. Mohr-Coulomb) is simple but disregards the important effect of the intermediate stress, whereas polyaxial strength models often provide nonunique solutions and are rarely available.

Another crucial element of the thermal breakout method is the ability to properly capture the thermal stress at the onset of breakout. Relying on the onset of breakout is an advantage over standard breakout stress analysis because it eliminates the need for characterizing the breakout width, a quantity resulting from a complicated nonlinear rock failure process. The stress estimation mostly relies on mechanics described using linear elasticity. We validated through laboratory experiments that acoustic emission monitoring



is a feasible method to capture the onset of wellbore failure. Appropriate thermal conduction model is also needed if direct measurements of the borehole wall temperature are not possible. Robust borehole wall temperature measurement and reliable technology to detect onset of breakout failure at in situ conditions are the essential capabilities for a successful thermal breakout borehole tool.

Acknowledgements Presented research was funded by U.S. Department of Energy, National Energy Technology Laboratory, under Award No. DE-FE0031688. We acknowledge the project team members: Thomas Doe, Cory Fehr, Timothy Kneafsey, Daniel Moos, Seiji Nakagawa, Jay Nopola and Jonny Rutqvist for their contributions to the theoretical development of the thermal breakout concept and insightful discussions. We also thank Insun Song for providing his experimental data

## References

- Akaike H (1974) A new look at the statistical model identification. IIEEE Trans Autom Control 19(6):716–723
- Al-Ajmi AM, Zimmerman RW (2005) Relation between the Mogi and the Coulomb failure criteria. Int J Rock Mech Min Sci 42(3):431–439
- Amadei B, Stephansson O (1997) Rock stress and its measurement. Chapman & Hall, Boca Raton
- Barton CA, Zoback MD, Burns KL (1988) In-situ stress orientation and magnitude at the Fenton Geothermal Site, New Mexico, determined from wellbore breakouts. Geophys. Res. Lett. 15(5):467–470
- Bažant ZP (1999) Size effect on structural strength: a review. Arch Appl Mech 69:703–725
- Carter BJ (1992) Size and stress gradient effects on fracture around cavities. Rock Mech Rock Eng 25:167–186
- Chang C, Haimson B (2000) True triaxial strength and deformability of the German Continental Deep Drilling Program (KTB) deep hole amphibolite. J Geophys Res 105(B8):18999–19013
- Chang C, McNeill LC, Moore JC, Lin W, Conin M, Yamada Y (2010) In situ stress state in the Nankai accretionary wedge estimated from borehole wall failures. Geochem Geophys Geosyst 11(12):1– 17. https://doi.org/10.1029/2010GC003261
- Clement C, Merrien-Soukatchoff V, Dunner C, Gunzburger Y (2009) Stress measurement by overcoring at shallow depths in a rock slope: the scattering of input data and results. Rock Mech Rock Eng 42:585–609
- Cornet FH (1983) Interpretation of hydraulic injection tests for in situ stress determination. In: Proceedings of hydraulic fracturing stress measurements. National Academy Press, pp 149–158
- Cornet FH (1986) Stress determination from hydraulic tests on preexisting fractures—the HTPF method. In: Proceedings of international symposium on rock stress and rock stress measurements. Centek Publ, pp 301–312
- Cornet FH, Burlet D (1992) Stress field determinations in France by hydraulic tests in boreholes. J Geophys Res 97(B8):11829–11849
- Cornet FH, Jianmin Y (1995) Analysis of induced seismicity for stress field determination and pore pressure mapping. Pure Appl Geophys 145(3):677–700
- Cornet FH, Doan ML, Fontbonne F (2003) Electrical imaging and hydraulic testing for a complete stress determination. Int J Rock Mech Min Sci 40:1225–1241

- Cuss RJ, Rutter EH, Holloway RF (2003) Experimental observations of the mechanics of borehole failure in porous sandstone. Int J Rock Mech Min Sci 40(5):747–761
- De Bree P, Walters J (1989) Micro/minifrac test procedures and interpretation for in situ stress determination. Int J Rock Mech Min Sci Geomech Abstr 26(6):515–521
- Drucker DC, Prager W (1952) Soil mechanics and plastic analysis or limit design. Q Appl Math 10(2):157–165
- Economides MJ, Nolte KG (2000) Reservoir stimulation. Wiley, Nwe York
- Ewy RT (1999) Wellbore-stability predictions by use of a modified Lade criterion. SPE Drill Complet 14:85–91
- Fjær E, Holt RM, Horsrud P, Raaen AM, Risnes R (2008) Petroleum related rock mechanics. Elsevier, New York
- Graham CC, Stanchits S, Main IG, Dresen G (2010) Comparison of polarity and moment tensor inversion methods for source analysis of acoustic emission data. Int J Rock Mech Min Sci 47(1):161–169
- Haimson B (2007) Micromechanisms of borehole instability leading to breakouts in rocks. Int J Rock Mech Min Sci 44(2):157–173
- Haimson B, Chang C (2000) A new true triaxial cell for testing mechanical properties of rock, and its use to determine rock strength and deformability of Westerly granite. Int J Rock Mech Min Sci 37(1):285–296
- Haimson B, Cornet FH (2003) ISRM suggested methods for rock stress estimation part 3: hydraulic fracturing (HF) and/or hydraulic testing of pre-existing fractures (HTPF). Int J Rock Mech Min Sci 40:1011–1020
- Haimson B, Kovacich J (2003) Borehole instability in high-porosity Berea sandstone and factors affecting dimensions and shape of fracture-like breakouts. Eng Geol 69(3):219–231
- Haimson B, Lee H (2004) Borehole breakouts and compaction bands in two high-porosity sandstones. Int J Rock Mech Min Sci 41(2):287–301
- Haimson B, Song I (1993) Laboratory study of borehole breakouts in Cordova Cream: a case of shear failure mechanism. Int J Rock Mech Min Sci Geomech Abstr 30(7):1047–1056
- Hakami E, Christiansson R (2011) Determination of in situ stress orientation by thermally induced spalling. Paper presented at the 12th ISRM Congress, Beijing, China
- Heidbach O, Tingay M, Barth A, Reinecker J, Kurfeß D, Müller B (2010) Global crustal stress pattern based on the World Stress Map database release 2008. Tectonophysics 482(1):3–15
- Hooker VE, Bickel DL (1974) Overcoring equipment and techniques used in rock stress determination. Tech Rep Circ 8618:USBM
- Ingraham MD, Issen KA, Holcomb DJ (2013) Response of Castlegate sandstone to true triaxial states of stress. J Geophys Res 118(2):536-552
- ISRM (1987) Method 3: suggested method for rock stress determination using a USBM-type drillhole deformation gauge. Int J Rock Mech Min Sci Geomech Abstr 24(1):63–68
- Jaeger JC, Cook NGW, Zimmerman RW (2007) Fundamentals of rock mechanics. Blackwell Publishing, Hoboken
- Jarosiński M (2005) Ongoing tectonic reactivation of the outer carpathians and its impact on the foreland: results of borehole breakout measurements in Poland. Tectonophysics 410(1):189–216
- Kalkan E (2016) An automatic P-phase arrival-time picker. Bull Seismol Soc Am 106(3):971–986
- Kirsch G (1898) Die Theorie der Elastizität und die Bedürfnisse der Festigkeitslehre. Zeitschrift des Verlines Deutscher Ingenieure 42:707
- Labuz JF, Bridell JM (1993) Reducing frictional constraint in compression testing through lubrication. Int J Rock Mech Min Sci Geomech Abstr 30(4):451–455
- Lade P, Duncan J (1975) Elastoplastic stress–strain theory for cohesionless soil. J Geotech Geoenviron 101:1037–1053



- Lee M, Haimson B (1993) Laboratory study of borehole breakouts in Lac du Bonnet granite: a case of extensile failure mechanism. Int J Rock Mech Min Sci Geomech Abstr 30(7):1039–1045
- Lee H, Haimson BC (2011) True triaxial strength, deformability, and brittle failure of granodiorite from the San Andreas fault observatory at depth. Int J Rock Mech Min Sci 48(7):1199–1207
- Lin H, Oh J, Canbulat I, Stacey TR (2020) Experimental and analytical investigations of the effect of hole size on borehole breakout geometries for estimation of in situ stresses. Rock Mech Rock Eng 53:781–798
- Lund B, Zoback MD (1999) Orientation and magnitude of in situ stress to 6.5 km depth in the Baltic Shield. Int J Rock Mech Min Sci 36(2):169–190
- Ma X, Haimson BC (2016) Failure characteristics of two porous sandstones subjected to true triaxial stresses. J Geophys Res 121(9):6477-6498
- Ma X, Ingraham MD (2018) On the applicability of Nadai and Mogi failure criteria to porous sandstones. Rock Mech Rock Eng 51:3835–3843
- Malinverno A, Saito S, Vannucchi P (2016) Horizontal principal stress orientation in the Costa Rica Seismogenesis Project (CRISP) transect from borehole breakouts. Geochem Geophys Geosyst 17(1):65–77
- Martin CD, Martino JB, Dzik EJ (1994) Comparison of borehole breakouts from laboratory and field tests. Paper presented at the Rock Mechanics in Petroleum Engineering, Delft, Netherlands. https:// doi.org/10.2118/28050-MS
- Meier T, Rybacki E, Reinicke A, Dresen G (2013) Influence of borehole diameter on the formation of borehole breakouts in black shale. Int J Rock Mech Min Sci 62:74–85
- Mogi K (1971) Fracture and flow of rocks under high triaxial compression. J Geophys Res 76(5):1255–1269
- Moos D, Zoback MD (1990) Utilization of observations of well bore failure to constrain the orientation and magnitude of crustal stresses: application to continental, deep sea drilling project, and ocean drilling program boreholes. J Geophys Res 95(B6):9305–9325
- Moos D, Zoback MD (1993) State of stress in the Long Valley caldera, California. Geology 21(9):837–840
- Nadai A (1950) Theory of flow and fracture of solids. McGraw-Hill, New York
- Nelder JA, Mead R (1965) A simplex method for function minimization. Comput. J. 7(4):308–313
- Nesetova V, Lajtai EZ (1973) Fracture from compressive stress concentrations around elastic flaws. Int J Rock Mech Min Sci Geomech Abstr 10(4):265–284
- Noda N, Hetnarski RB, Tanigawa Y (2003) Thermal stresses. Taylor & Francis, London
- Nopola J, Voegeli S, Knight J, Artz T, Jones M (2020) Initial field testing in the deep subsurface for the thermal breakout project for measuring in situ stress. Paper presented at the 54th U.S. Rock Mechanics/Geomechanics Symposium, physical event cancelled
- Peška P, Zoback MD (1995) Compressive and tensile failure of inclined well bores and determination of in situ stress and rock strength. J Geophys Res 100(B7):12791–12811

- Serata S, Sakuma S, Kikuchi S, Mizuta Y (1992) Double fracture method of in situ stress measurement in brittle rock. Rock Mech Rock Eng 25:89–108
- Siren T, Suikkanen J, Heikkinen E, Valli J, Hakala M (2015) Determining the in situ stress with thermally induced borehole breakout. Paper presented at the 13th ISRM International Congress of Rock Mechanics, Montreal, Canada
- Sjöberg J, Christiansson R, Hudson J (2003) Isrm suggested methods for rock stress estimation-part 2: overcoring methods. Int J Rock Mech Min Sci 40(7):999–1010
- Song I, Haimson BC (1997) Polyaxial strength criteria and their use in estimating in situ stress magnitudes from borehole breakout dimensions. Int J Rock Mech Min Sci 34(3):116e1-116e16
- Stephansson O (1983) Sleeve fracturing for rock stress measurement in boreholes. in: Proc. Int. Symp. Essais en Place, In Situ Testing, Paris, vol 2, pp 571–578
- Stephens G, Voight B (1982) Hydraulic fracturing theory for conditions of thermal stress. Int J Rock Mech Min Sci Geomech Abstr 19(6):279–284
- Voegeli S, Nopola J, Moos D, Doe T (2021) Deterministic and statistical modeling of a new thermal breakout technology for measuring the maximum horizontal in-situ stress. SPE J 26:83–91. https://doi.org/10.2118/201195-PA
- Wileveau Y, Cornet FH, Desroches J, Blumling P (2007) Complete in situ stress determination in an argillite sedimentary formation. Phys Chem Earth 32:866–878
- Worotnicki G (1993) CSIRO triaxial stress measurement cell. In: Hudson JA (ed) Comprehensive rock engineering, vol 3. Pergammon Press, Oxford, pp 329–394
- Zang A, Christian Wagner F, Stanchits S, Dresen G, Andresen R, Haidekker MA (1998) Source analysis of acoustic emissions in Aue granite cores under symmetric and asymmetric compressive loads. Geophys J Int 135(3):1113–1130
- Zhou S (1994) A program to model the initial shape and extent of borehole breakout. Comput Geosci 20(7):1143–1160
- Zoback ML (1992) First- and second-order patterns of stress in the lithosphere: the World Stress Map project. J Geophys Res 97(B8):11703–11728
- Zoback MD (2007) Reservoir geomechanics. Cambridge University Press, Cambridge
- Zoback MD, Moos D, Mastin L, Anderson RN (1985) Well bore breakouts and in situ stress. J Geophys Res 90(B7):5523–5530
- Zoback MD, Barton CA, Brudy M, Castillo DA, Finkbeiner T, Grollimund BR, Moos DB, Peška P, Ward CD, Wiprut DJ (2003) Determination of stress orientation and magnitude in deep wells. Int J Rock Mech Min Sci 40:1049–1076

**Publisher's Note** Springer Nature remains neutral with regard to jurisdictional claims in published maps and institutional affiliations.

